



Cite this: *Nanoscale*, 2022, **14**, 6811

## Fast and efficient electrochemical thinning of ultra-large supported and free-standing MoS<sub>2</sub> layers on gold surfaces†

Nicolli de Freitas,<sup>a</sup> Bianca R. Florindo,<sup>ID a</sup> Vitória M. S. Freitas,<sup>a</sup> Maria H. de O. Piazzetta,<sup>a</sup> Carlos A. Ospina,<sup>a</sup> Jefferson Bettini,<sup>a</sup> Mathias Strauss,<sup>ID a,b</sup> Edson R. Leite,<sup>a,d</sup> Angelo L. Gobbi,<sup>ID a</sup> Renato S. Lima<sup>ID a,b,c,d</sup> and Murilo Santhiago<sup>ID \*a,b</sup>

Molybdenum disulfide (MoS<sub>2</sub>) is a very promising layered material for electrical, optical, and electrochemical applications because of its unique and outstanding properties. To unlock its full potential, among different preparation routes, electrochemistry has gained interest due to its simple, fast, scalable and simple instrumentation. However, obtaining large-area monolayer MoS<sub>2</sub> that will enable the fabrication of novel electronic and electrochemical devices is still challenging. In this work, we reported a simple and fast electrochemical thinning process that results in ultra-large MoS<sub>2</sub> down to monolayer on Au surfaces. The high affinity of MoS<sub>2</sub> by Au surfaces enables the removal of bulk layers while preserving the first layer attached to the electrode. With a proper choice of the applied potential, more than 90% of the bulk regions can be removed from large-area MoS<sub>2</sub> crystals, as confirmed by atomic force microscopy, photoluminescence, and Raman spectroscopy. We further address a set of contributions that are helpful to elucidate the features of MoS<sub>2</sub>, namely, the hyphenation of electrochemistry and optical microscopy for real-time observation of the thinning process that was revealed to occur from the edges to the center of the flake, an image treatment to estimate the thinning area and thinning rate, and the preparation of free-standing MoS<sub>2</sub> layers by electrochemically thinning bulk flakes on microhole-structured Ni/Au meshes.

Received 25th January 2022,  
Accepted 14th March 2022

DOI: [10.1039/d2nr00491g](https://doi.org/10.1039/d2nr00491g)  
[rsc.li/nanoscale](http://rsc.li/nanoscale)

## Introduction

2D materials have attracted a lot of attention in recent years due to their interesting optical,<sup>1</sup> electronic,<sup>2</sup> and electrochemical properties.<sup>3</sup> Among the several 2D materials, the family of transition metal dichalcogenides (TMDs) shows a broad range of remarkable electronic properties that can be associated with their many chemical compositions and structural phases.<sup>4</sup> This emerging class of 2D materials is being studied from fundamental aspects toward a plethora of applications. For instance, such materials have been used in elec-

tronic micro/nano devices,<sup>5</sup> optical sensors,<sup>6</sup> energy storage,<sup>7</sup> biosensors,<sup>8</sup> and electrocatalysis,<sup>9</sup> to name a few. In particular, MoS<sub>2</sub> is abundant on earth and one of the most studied examples of TMDs due to its suitable electronic and optical properties.<sup>10</sup> Thus, the preparation of large-area and ultrathin 2D layers is extremely important to explore the huge potential of MoS<sub>2</sub>.

In the last years, continuous efforts by researchers have led to development of different methods for the production of ultrathin layered materials.<sup>11</sup> These methods can be classified in two main categories, namely, top-down and bottom-up approaches.<sup>12</sup> Top-down methods are based on applying an external force to break the weak van der Waals interaction that occurs between the sheets. Examples of these methods include mechanical exfoliation and intercalation with ions and molecules. Mechanical exfoliation can produce large MoS<sub>2</sub> monolayers, however, the process is time consuming and scalability still require future efforts.<sup>13–15</sup> Intercalation methods,<sup>16</sup> on the other hand, can exfoliate large amounts of TMDs and induce phase change, for example, MoS<sub>2</sub> changes from semiconductor (2H phase) to conductor (1T phase) when using *n*-butyl-lithium as intercalation source.<sup>17</sup> In addition, intercalation is

<sup>a</sup>Brazilian Nanotechnology National Laboratory, Brazilian Center for Research in Energy and Materials, Campinas, São Paulo 13083-970, Brazil.

E-mail: murilo.santhiago@lnnano.cnpm.br

<sup>b</sup>Federal University of ABC, Santo André, São Paulo 09210-580, Brazil

<sup>c</sup>Institute of Chemistry, University of Campinas, Campinas, São Paulo 13083-970, Brazil

<sup>d</sup>São Carlos Institute of Chemistry, University of São Paulo, São Carlos, São Paulo 09210-580, Brazil

† Electronic supplementary information (ESI) available: AFM images, electrochemical experiments and additional photos. See DOI: <https://doi.org/10.1039/d2nr00491g>

able to hasten succeeding exfoliation, due to expansion of the interlayer distance that weakens van der Waals forces between two adjacent layers. Despite the advantages, the preparation of monolayers with large lateral sizes by intercalation methods still remains challenging. Bottom-up synthesis of monolayer MoS<sub>2</sub> combines Mo and S precursors to produce monolayers of different lateral sizes on substrates.<sup>18</sup> Yang *et al.* reported a chemical vapor deposition (CVD) process to synthesize centimeter-scale MoS<sub>2</sub> monolayers catalysed by sodium on glass.<sup>19</sup> However, CVD grown is time consuming and demands high temperature for the synthesis of monolayer TMDs.

Among the preparation methods of atomically thin TMDs,<sup>20–23</sup> electrochemical exfoliation has been successfully employed for preparing atomically thin TMDs due to its advantages, such as, high yield, simple instrumentation, mild conditions and fast process.<sup>24–26</sup> Moreover, the exfoliation conditions can be tuned with simply adjusting the applied voltage or current.<sup>27</sup> There are two main electrochemical approaches to exfoliate MoS<sub>2</sub> into atomically thin layers, namely, cathodic and anodic exfoliation.<sup>24,25</sup> Cathodic exfoliation occurs due to intercalation of ions to produce high-yield and phase-pure nanosheets.<sup>28</sup> In its turn, the anodic process to obtain few to monolayer of MoS<sub>2</sub> can be done by clamping the macroscopic bulk crystal to a conductive clip<sup>29</sup> or transferring bulk MoS<sub>2</sub> onto electrically conductive substrates.<sup>30</sup> In the first approach, exfoliated sheets with lateral size in the order of 5–50 µm are released from the electrode and can be suspended on the electrolyte when a high voltage, *i.e.* 10 V, is applied.<sup>31</sup> The second route involves the transfer of bulk MoS<sub>2</sub> onto conductive substrates followed by an electrochemical treatment of the electrode to reduce the number of the layers down to a monolayer. In this method, conductive materials such as TiN and Pt have been used to thin bulk MoS<sub>2</sub> down to monolayer level using voltammetry.<sup>30,32,33</sup> However, the lateral

sizes of MoS<sub>2</sub> are still limited when compared with other methods.

In this work, we reported a simple and fast electrochemical thinning process of MoS<sub>2</sub> on gold surfaces enabling the preparation of ultra-large monolayers. Bulk MoS<sub>2</sub> flakes are transferred onto gold substrates and thinned down to monolayer using an electrochemical route. We took advantage of the high binding energy between MoS<sub>2</sub> and gold surfaces to minimize lixiviation of the 2D material during the electrochemical process. The process is simple, fast, and enables the preparation of ultra-large MoS<sub>2</sub> monolayers, the largest reported so far by electrochemical routes. The thinned flakes were characterized by raman spectroscopy, atomic force microscopy and photoluminescence experiments, thus confirming the monolayer nature of the investigated 2D material. Hyphenation of electrochemistry and optical microscopy allowed us real time observation of the thinning process. In addition, an alternative image treatment was used to calculate the thinning rate and thinned area, the later reached 90–100% at optimized conditions. Finally, in order to expand the possibilities of the method, we demonstrated for the first time the electrochemical thinning process using flexible gold meshes containing microholes, which enabled preparation of free-standing MoS<sub>2</sub> layers. The proposed method opens up the possibility to study optical, mechanical, and electrochemical properties of ultra-large area MoS<sub>2</sub>.

## Experimental

### Preparation of thin-film electrodes

Thin-film electrodes were prepared by depositing Cr (20 nm) and Au (150 nm), respectively, on glass slides using an electron beam system (AJA International). Before receiving the MoS<sub>2</sub> flakes, the substrate underwent a two-stage cleaning process. First, a wet cleaning procedure using acetone, isopropanol, and water was performed. The second stage consisted of cleaning the surface using oxygen plasma (Dienner nano) for 10 min at a power of 30%, pressure of 0.3 mBar and temperature of 100 °C. After the cleaning process, bulk MoS<sub>2</sub> crystals (SPI supplies, PA, USA) were mechanically exfoliated using the “scotch-tape” method and transferred onto the clean gold electrodes by using two approaches.

In the first approach, the number of MoS<sub>2</sub> layers was reduced by successive mechanical exfoliation steps using a tape (Nitto). Next, the tape containing bulk flakes was attached on the electrodes and 350 g weight were put on the top of the tape, resulting in pressure of 1.8 kPa. The tape was kept into contact with the electrode for 5 h. Afterward, the tape was removed and the electrode was used in the electrochemical experiments. In the second approach, we melted sucrose (Synth, SP, Brazil) at 200 °C until becoming brownish-yellow. Next, we dropped the melted sugar on the tape containing previously exfoliated bulk MoS<sub>2</sub> flakes. After solidification of sugar, the resulting solid piece was peeled off and positioned on the gold substrate. Finally, the sugar was washed with de-



Murilo Santhiago

Dr. Murilo Santhiago is a researcher at the Brazilian Nanotechnology National Laboratory (LNNano), located in the Brazilian Center for Research in Energy and Materials (CNPEM) in Campinas, SP, Brazil. He received his PhD in chemistry from University of Campinas (UNICAMP) in 2014. His current research interest are flexible electrochemical nanodevices, paper-based devices, micro-nanofabrication and 2D

materials toward energy, environmental, and health fields. One of his goals is to stimulate student's creativity to guide them to solve relevant problems of our society by exploring the amazing field of nanotechnology.

ionized water leaving the bulk  $\text{MoS}_2$  flakes on the substrate. The edges of the electrodes were protected by applying an insulating resin. Single-flake microelectrodes were prepared by applying the insulating resin on the entire gold film leaving uncovered only the selected  $\text{MoS}_2$  flake.

### Fabrication of the micropatterned gold-coated nickel meshes

Microhole-structured meshes of Ni were fabricated through photolithography and electrodeposition processes. The molds required for the following electrodeposition of Ni were manufactured on  $25\text{ cm}^2$  glass slides coated with metallic thin films of Cr (25 nm) and Au (200 nm) *via* sputtering (Orion 8 Phase II-J, AJA International). Photoresist patterns were engraved on these molds by photolithography from dark field masks with an array of micropores containing a nominal diameter of 20  $\mu\text{m}$ . These masks were achieved *via* direct laser writing ( $\mu\text{PG101}$ , Heidelberg). In practice, the metal-coated glass substrates were left on a hot plate at 120  $^\circ\text{C}$  during 10 min for dehydration. Then, the adhesion promoter hexamethyldisilazane (HMDS) and photoresist AZ50XT were sequentially deposited by spin coating (Headway Research) at distinct conditions, namely, rotation of 4000 rpm (30 s) for the HMDS and 2000 (20 s) and 3400 rpm (5 s) for the photoresist. The HMDS-coated slides were pre-baked at 120  $^\circ\text{C}$  for 10 min, whereas this step for the photoresist-coated slides relied on a ramp from 50 to 112  $^\circ\text{C}$  for 30 min. The exposure to ultraviolet light (UV) was conducted in the photoaligner (MJB3 photoaligner, Karl Suss) during 150 s under a power of  $9.5\text{ mW cm}^{-2}$  using a dark field mask as aforesaid. Next, the photoresist was developed in AZ K400 1 : 3 v/v in solvent for approximately 2.5 min. The photoresist film thickness was around 25  $\mu\text{m}$  according to the optical profilometer (Dektak 150 Veeco, Bruker).

The electrochemical growth of Ni was made in an electroplating bath (Electrogalvano). The dc power supplier (HP E3631A, Agilent Technologies) provided a current of 250 mA for 60 min, whereas cycling washes using deionized water were made every 15 min. The resulting Ni film reached a thickness of approximately 20  $\mu\text{m}$ . The photoresist was removed *via* immersion in acetone. After, the excesses of Cr/Au were removed from the meshes by dipping the glass substrates into their respective etching bathes. Finally, the mesh was washed with Extran® and isopropanol, followed by drying under nitrogen flow. To serve as raw electrode material, Au (1.5  $\mu\text{m}$ ) was deposited onto the Ni meshes by electrodeposition as well. This procedure was accomplished at 65  $^\circ\text{C}$  applying a current density of  $0.3\text{ A dm}^{-2}$  for 10 min.

### Electrochemical measurements

Electrochemical experiments were done using a three-electrode electrochemical cell using Ag/AgCl as reference, glassy carbon as counter electrode and microfabricated Au films as working electrodes. The electrochemical measurements were done using a PGSTAT-204 potentiostat model from AUTOLAB (Eco Chemie, Netherlands) interfaced with a computer and controlled by the NOVA 2.1 software. In a typical electrochemical thinning process, chronoamperometry tests were proceeded

applying 1.5 V *vs.* Ag/AgCl for certain time. Next, the potential was scanned from  $-0.1$  to  $0.5\text{ V}$  at  $10\text{ mV s}^{-1}$  for ten cycles using cyclic voltammetry. This process was done to reduce the Au oxide formation after chronoamperometry. The supporting electrolyte was  $0.5\text{ M H}_2\text{SO}_4$  (Sigma-Aldrich, SP, Brazil). For comparison, electrochemical thinning was also performed on fluorine doped tin oxide (FTO) electrodes.

### Characterization

Topographic images were acquired using atomic force microscopy (AFM, ParkSystems NX-10) in  $\text{N}_2$  atmosphere applying the tapping mode of AFM with a FMR probe (NanoSensors), working with 75 kHz as nominal resonant frequency and  $2.8\text{ N m}^{-1}$  as constant nominal springs. The acquired images were treated on Gwyddion software. Raman spectra were taken with 532 nm laser and  $50\times$  objective lens (XploRA Plus Horiba). Raman mapping was acquired with a step of 0.75  $\mu\text{m}$  in the range of 300 to 500  $\text{cm}^{-1}$ . Photoluminescence (PL) was also measured using XploRA Plus Horiba equipment with 532 nm laser in the range of 550 to 800 nm using a  $50\times$  objective lens. X-Ray photoelectron spectroscopy (XPS) was carried out with a Thermo Scientific K $\alpha$  spectrometer (U.K.). Optical images before and after the thinning process were taken using a Zeiss Microscope Icc5 at different magnifications. For the electrochemistry-microscopy experiments a miniaturized electrochemical cell was mounted on the mechanical stage of the microscope. A perforated polydimethylsiloxane (PDMS) layer was placed on the top of the gold electrode to define the volume of the cell. Next, Ag/AgCl and a platinum wire were used as reference and counter electrodes. The volume of  $\text{H}_2\text{SO}_4$  in the cell was adjusted to preserve the focus of the  $\text{MoS}_2$  flake. Image J software was used to calculate the thinned area. First, the images obtained by optical microscopy were split in RGB colors, followed by contrast/brightness adjustment. Finally, a threshold was applied to enable the measurement of thinned areas. Scanning electron microscopy (SEM) and energy dispersive X-ray spectroscopy (EDS) images were obtained using a Helios Nanolab 660 (Thermo Fischer Scientific).  $\text{MoS}_2$  samples were analyzed in a Double Aberration-Corrected Transmission Electron Microscope (TEM), Titan Cubed Themis, of the LNNano, at 80 kV, in Scanning Transmission Electron Microscopy (STEM) mode. A camera length of 115 mm and a semi-converge angle of 17.9 mrad were used for illuminating the samples and a High-Angle Annular Dark-Field (HAADF) detector for acquiring the High-Resolution STEM (HRSTEM) images. The image was obtained in a cracked region on the center of the microhole-structured electrode.

## Results and discussion

Mechanical exfoliation using scotch-tape was performed to decrease the number of layers of natural  $\text{MoS}_2$  flakes. We tested two approaches to transfer the flakes onto Au electrodes.

The first one consisted of mechanical exfoliation followed by putting the tape containing the flakes in contact with micro-fabricated Au substrates for approximately 5 h in the clean room. Large flakes are transferred using this approach, however, the transfer yield is low. In the second approach we adapted the use of sucrose<sup>34</sup> to successfully increase the trans-

fer yield. Using this route, the number of transferred flakes was significantly higher and their lateral dimensions were larger. An additional advantage is that residual sucrose can be washed away using water, avoiding the use of organic solvents on the electrode. After that, the substrates containing the bulk MoS<sub>2</sub> flakes were used as working electrodes in the electrochemical experiments. It is important to mention that regardless of the route used, the flakes were thinned in the same manner.

Fig. 1a shows a scheme of three-electrode cell used in the experiments. After electrochemical oxidation the number of MoS<sub>2</sub> layers is gradually reduced to a monolayer, as schematically shown in Fig. 1b. Fig. 1c and d shows pictures of the MoS<sub>2</sub> flakes transferred using sucrose before and after the electrochemical step, respectively. Remarkably, ultra-large MoS<sub>2</sub> flakes were thinning down to monolayer using the electrochemical process on Au electrodes. The color of the MoS<sub>2</sub> flakes changed from a blue/grey color (which represents bulk crystals) to yellowish, indicating that the number of layers has been reduced. It is possible to confirm the regions with few layers and monolayers *via* characterization by atomic force microscopy, photoluminescence and raman spectroscopy.

Optical microscopy was used as first inspection of the samples. Fig. 2a and b shows MoS<sub>2</sub> flake before and after the electrochemical step, respectively. The color change from light grey to brownish yellow indicates that the thinning process was well succeeded. In addition, more than 90% of bulk regions were removed by treating the images in Fig. 2a and b using image J software, as it will be shown ahead. The thickness of the flake before and after the thinning process was measured using AFM, as shown in Fig. 2c and d, respectively.

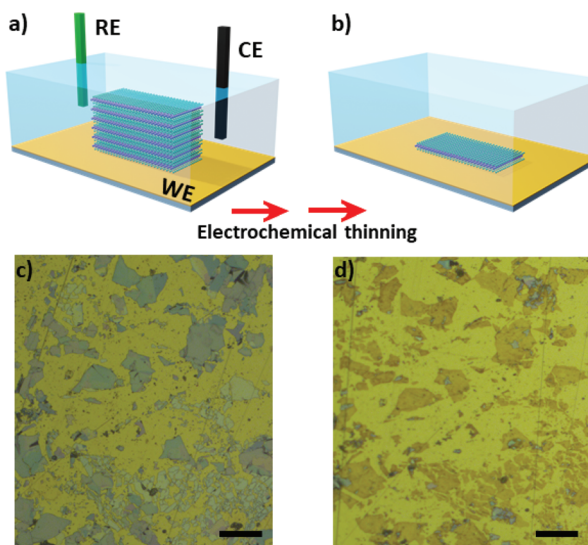


Fig. 1 (a) Schematic view of the three-electrode cell. (b) Illustrative image of the electrode after electrochemical thinning process showing that bulk flakes are thinned down to monolayer. Optical microscope images of the electrodes containing MoS<sub>2</sub> flakes before (c) and after (d) electrochemical experiments. Scale bars are 100  $\mu$ m.

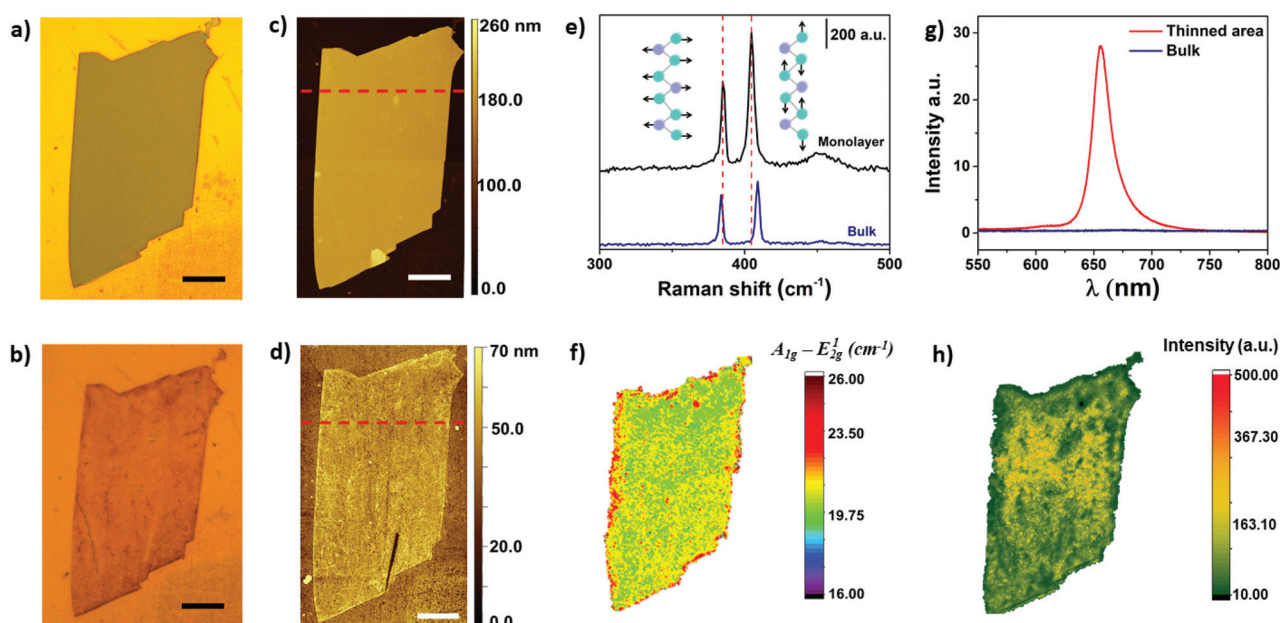


Fig. 2 Optical (a, b) and AFM images (c, d) of MoS<sub>2</sub> flakes before (a, c) and after (b, d) electrochemical thinning. Scale bars are 20  $\mu$ m. (e) Raman spectra of bulk and monolayer regions. (f) Raman map of electrochemically thinned MoS<sub>2</sub> flake. (g) Photoluminescence (PL) spectra of thinned and bulk areas. (h) PL map of the electrochemically thinned MoS<sub>2</sub> crystal. PL intensity in (g) and (h) was normalized by  $A_{1g}$  mode.

The thickness of the flake illustrated in Fig. 2c was initially 143 nm, thus confirming the bulk nature of MoS<sub>2</sub>. The thickness of bulk flakes on gold substrates were found in the range of 100–500 nm. After the electrochemical process, height profiles indicated that MoS<sub>2</sub> edges were thicker than basal plane (Fig. S1†). The thickness of inner regions of the flake was 0.8 nm, which is close to a monolayer.

Raman spectroscopy is commonly used to verify the number of MoS<sub>2</sub> layers. The E<sup>1</sup><sub>2g</sub> (in plane vibration) and A<sub>1g</sub> (out-of-plane) Raman-active modes of 2H MoS<sub>2</sub> can be detected in the range of 380 to 410 cm<sup>-1</sup>, approximately.<sup>35,36</sup> In addition, the frequency difference between E<sup>1</sup><sub>2g</sub> and A<sub>1g</sub> can be used to monitor layer thickness (1 to 5 layers).<sup>37</sup> Fig. 2e shows representative Raman spectra of a MoS<sub>2</sub> flake before and after electrochemical thinning. As can be observed, the frequency difference of the flake decreased from 25 cm<sup>-1</sup> (bulk) to less than 20 cm<sup>-1</sup> (monolayer). The Raman map illustrated in Fig. 2f shows a very homogeneous frequency difference on the basal plane, indicating that bulk layers were thinned down to monolayer. The red color observed on the edges suggest the presence of bulk residues, which are in agreement with the AFM results. We extended the wavenumber range in the Raman experiments to verify some additional information. Fig. S2† shows the Raman spectra in the range of 100 up to 1000 cm<sup>-1</sup>. We did not observe peaks in the range of 150 to 350 cm<sup>-1</sup>, indicating that no phase transition from 2H to 1T occurred after thinning.<sup>38</sup>

Photoluminescence experiments were also performed on bulk and electrochemically thinned MoS<sub>2</sub> materials. The PL intensity of MoS<sub>2</sub> is drastically increased when number of layers is reduced down to a monolayer.<sup>39,40</sup> Such difference is associated with the electronic band structure of MoS<sub>2</sub> that changes from indirect (bulk) to direct band-gap structure

(monolayer). In addition, it has been reported that emission of photons with energy of ~1.9 eV are associated with the presence of MoS<sub>2</sub> monolayers.<sup>39</sup> Fig. 2g shows the PL spectra of MoS<sub>2</sub> before and after the electrochemical thinning process. The spectrum shows peaks at 656 and 607 nm than can be associated with the presence of excitons A and B from the Brillouin zone, respectively. Moreover, a long low-energy tail can also be observed in Fig. 2g for the electrochemically thinned MoS<sub>2</sub> that can be attributed to the presence of trions.<sup>41</sup> The later are negatively charged excitons (A<sup>-</sup>) centered at approximately 666 nm and observed in monolayer MoS<sub>2</sub>.<sup>42</sup> Therefore, the high intensity of the A exciton after the electrochemical thinning process further indicates that the number of layers were thinned down to a monolayer. In addition, the peak position attributed to A exciton, located at 656 nm (~1.89 eV), is in good agreement with the values reported in literature for monolayer MoS<sub>2</sub>.<sup>43</sup> The PL map illustrated in Fig. 2h shows a more homogeneous PL intensity in the center region of the exfoliated flake. At the edges, the PL intensity was lower due to the presence of bulk residues, as described above.

The thinning process was investigated by cyclic voltammetry (CV) using microelectrodes to observe the contribution of a single flake. Fig. 3a depicts the CVs of a bare microfabricated Au electrode. In the anodic direction the current increases at approximately 1.3 V, which is consistent with the potential where the oxidation of gold take place.<sup>45</sup> In the back scan, two peaks were observed at ~0.9 V and 0.6 V. The peak at 0.9 V is attributed to the reduction of the gold oxide formed during the anodic scan while the peak at 0.6 V is due to reduction of the Cr that arises from the adhesion layer. It was demonstrated that the electrolyte can reach the adhesion layer due to the presence of pinholes on the gold film.<sup>46</sup> In the presence of MoS<sub>2</sub> a large oxidation peak can be observed in the cyclic vol-

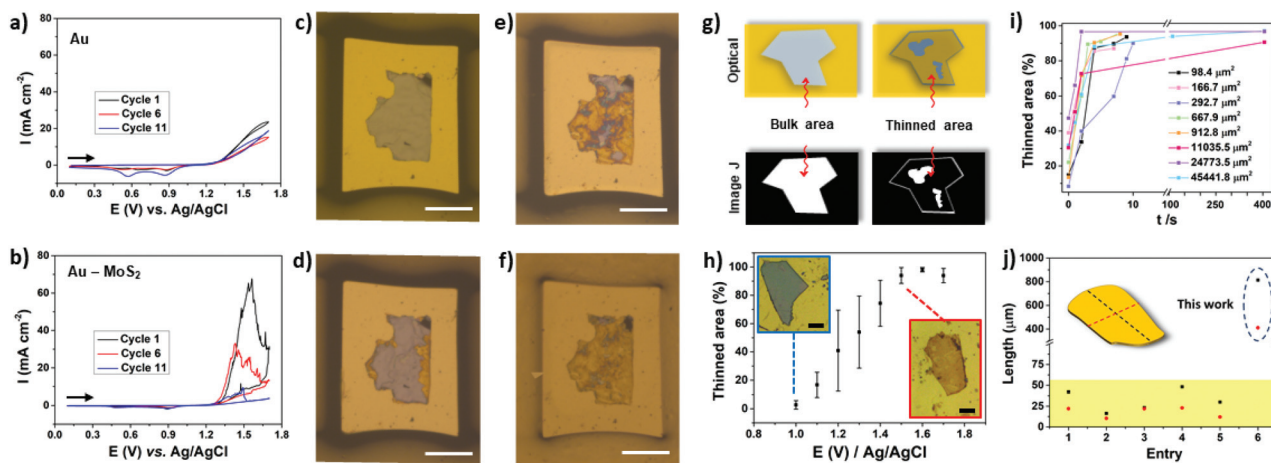


**Fig. 3** Cyclic voltammograms (CVs) obtained for (a) Au and (b) Au–MoS<sub>2</sub> ( $t_{\text{flake}} = 345$  nm) electrodes in 0.5 M H<sub>2</sub>SO<sub>4</sub> at 50 mV s<sup>-1</sup>. The current was normalized by the geometric area of the electrodes. Stereomicroscope images of the electrodes (Au–MoS<sub>2</sub>) before the experiment (c) and after cycle 1 (d), cycle 6 (e) and cycle 11 (f). The area and thickness of the MoS<sub>2</sub> flake are 19 714  $\mu\text{m}^2$  and 345 nm, respectively. The scale bars in c–f are 100  $\mu\text{m}$ . (g) Scheme illustrating the treatment by image J software. (h) Influence of the applied potential on thinned area. Scale bars are 25  $\mu\text{m}$ . (i) Thinned area versus time. (j) Comparison of lateral flake sizes with different works in literature. Red and black dashed lines represent width and length, respectively. Entry: [1],<sup>31</sup> [2, 3],<sup>30</sup> [4],<sup>32</sup> and [5].<sup>44</sup>

tammogram, as can be observed in Fig. 3b. The peak current at approximately 1.5 V decreases with the cycling process due to the thinning process. As can be observed in Fig. 3c–f, the thinning process advances as the number of cycles increases. The decrease in peak current was found to be dependent on the thickness of the bulk MoS<sub>2</sub> flake in the range of 60 to 480 nm. A single 60 nm thick MoS<sub>2</sub> flake was almost completely thinned on the first cycle, as illustrated in Fig. S3.† By comparing the peak current for microelectrodes containing 345 and 480 nm thick single flakes with very similar areas, as illustrated in Fig. 3b and S3,† it is possible to observe that more cycles are necessary for the thinning process using the thicker flake.

Next, we focused our study to obtain more information of the thinning process using image treatment. By obtaining optical images before and after the electrochemical process it is possible to investigate the influence of the applied potential and thinning time over the efficacy of the electrochemical treatment. The colors of bulk and electrochemically thinned MoS<sub>2</sub> after image treatment were converted to white and black, respectively, as schematically illustrated in Fig. 3g. This process allowed us to estimate the thinned area at different experimental conditions. Fig. 3h shows the influence of the applied potential. At 1.0 V, the thinned process was observed only at the edges of the flakes, resulting in low thinned areas, less than 10%. As the applied potential was moved up to 1.7 V, the thinned area was remarkably increased. The curve reached a plateau in 1.5 V, resulting in thinned areas higher than 90%. Fig. 3i shows that the electrochemical process is fast, reaching 90% of thinned areas in less than 60 s for different flake sizes. As can be observed, larger flakes need more time to reach higher thinning yields. Fig. S4† shows an ultra-large MoS<sub>2</sub> flake thinned by the proposed electrochemical route. Based on these results, oxidation time plays an important role to obtain large-area thinned MoS<sub>2</sub> with minimum of bulk residues on the basal plane. Notably, the electrochemical process over large areas resulted in thinned areas with high yield. As it can be observed in Fig. 3j, remarkably, the lateral dimensions of the thinned MoS<sub>2</sub> flake presented in this work surpasses the most recent works. We tested the thinning process on FTO using similar conditions but some regions of MoS<sub>2</sub> were lixivated (Fig. S5†).

Hyphenation of techniques allows us to obtain complementary, *in situ*, and real-time information about the electrochemical thinning process that occurs on the MoS<sub>2</sub> flake deposited on Au electrodes. A compact electrochemical cell was mounted on the mechanical stage of an optical microscope using miniaturized reference and counter electrodes, as schematically shown in Fig. 4a. An representative chronoamperometric curve is presented in Fig. 4b. It is observed that the electrochemical thinning process is ultra-fast, as illustrated in the sequence of frames shown in Fig. 4c. The thinned flakes can be clearly visualized by color changes from light grey (bulk MoS<sub>2</sub>) to yellowish (monolayer MoS<sub>2</sub>). The arrows, in the image indicate that the thinning process start at the edges and rapidly moves into direction to the central regions of the flake.

When the current decreased to their minimum values in the chronoamperograms more than 90% of the flake reached few to monolayer. Fig. 4d and e shows the pictures of the flake before and after the electrochemical process on Au electrodes, respectively. The Raman maps clearly illustrates that the thinning process mostly generates monolayer regions on the basal plane, illustrated by the green regions on the map shown in Fig. 4f.

By considering the microscopy-electrochemistry and previous characterization studies it is possible to draw the following scenario for the thinning process, as schematically shown in Fig. 4g. The bulk MoS<sub>2</sub> crystals adsorbed onto Au electrodes are initially electrochemically thinned at the flake edges. The following reaction is proposed to occur on the material:<sup>44</sup>



We also investigated the influence of dissolved oxygen over the thinning process. MoS<sub>2</sub> flakes were thinned in the same extend in the presence and absence of O<sub>2</sub> in electrolyte solution, as shown in Fig. S6.† One should note that in the potential region used to promote the thinning process with high yield, *i.e.* 1.5–1.7 V, O<sub>2</sub> bubbling also occurs on gold electrodes using H<sub>2</sub>SO<sub>4</sub> as electrolyte.<sup>47</sup> As the thinning process advances into inner regions of the flake a remaining bulk region is left on the edges. The bulk region can be seen on images illustrated in Fig. 4c after 22 s (dark regions at the edges) and it was further confirmed by AFM and Raman experiments. As the electrochemical oxidation proceeds, the bulk island on the center region of the flake is slowly thinned resulting in a terrace that is predominately monolayer. In addition, we investigated the impact of the thickness of the bulk flakes before the thinning process on the width of the bulk regions left on the edges after the electrochemical step. The width of this region increases as a function of the thickness of the bulk flake, as illustrated in Fig. S7.† Thus, in order to minimize the bulk region on the edges thinner flakes should be used.

The surface chemistry of the electrochemically thinned MoS<sub>2</sub> layers at different times was assessed by X-ray photoelectron spectroscopy (XPS), as shown in Fig. 5. The Mo 3d spectra of MoS<sub>2</sub> before electrochemical thinning, illustrated in Fig. 5a, revealed peaks at around 229.5, 232.6 and 235.7 eV that can be attributed to Mo<sup>4+</sup> 3d<sub>5/2</sub>, Mo<sup>4+</sup> 3d<sub>3/2</sub> and Mo<sup>6+</sup> 3d<sub>3/2</sub>. The S 2p<sub>1/2</sub> and S 2p<sub>3/2</sub> were found at 163.5 and 162.3 eV in the S region of Fig. 5a, as reported.<sup>31,48</sup> The resulting Mo and S peaks are characteristic of MoS<sub>2</sub> at the 2H phase with minimal oxidation, less than 2% for Mo<sup>6+</sup>. Fig. 5b–d reveals the evolution of XPS spectra at different electrochemical thinning times, from 5 up to 240 s. We noticed that percentage of Mo<sup>6+</sup> increased to 6% after 240 s of thinning time, indicating partial oxidation of MoS<sub>2</sub> after electrochemical experiments. Despite this increase, the percentage of Mo<sup>6+</sup> is considered low when compared with other works.<sup>49</sup> At the S region, we observed a small peak at 164.5 eV,<sup>50</sup> indicating the presence of bridging S<sub>2</sub><sup>2-</sup> and/or S<sup>2-</sup> in MoS<sub>x</sub> on the surface at 20 s and 240 s.

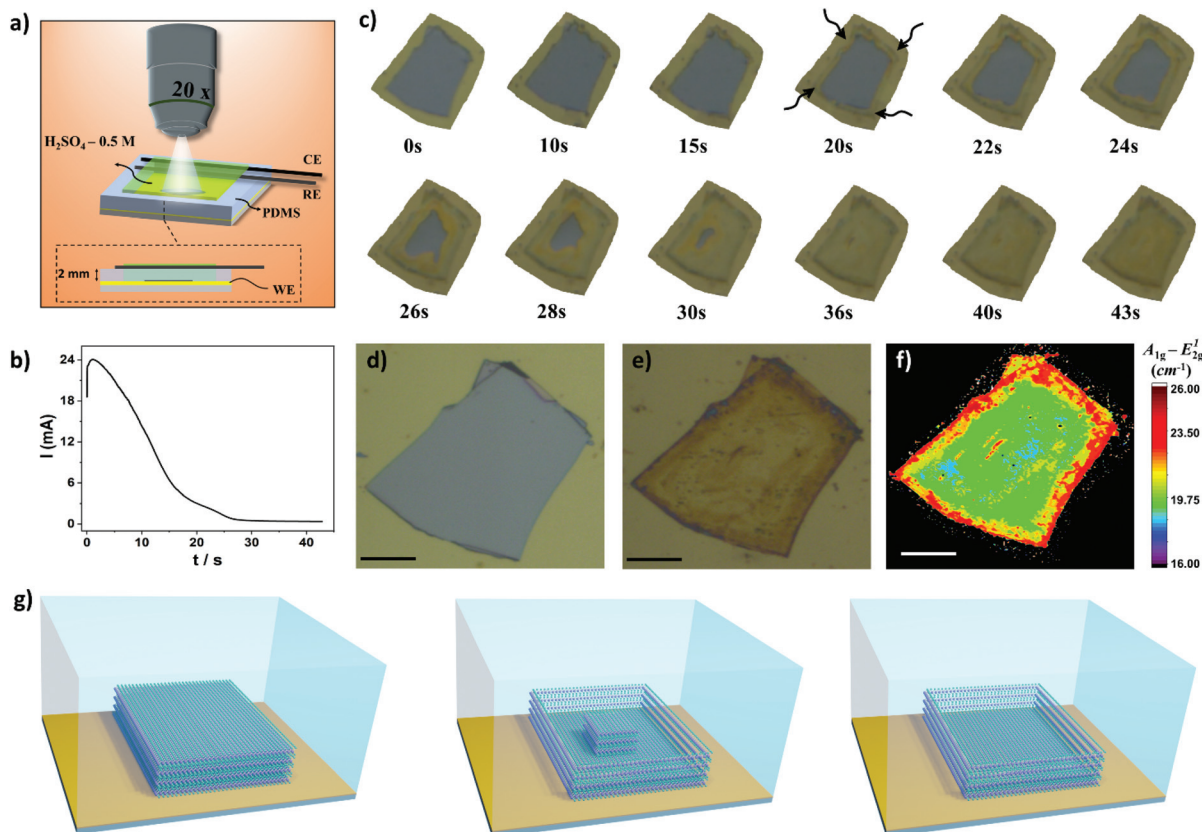


**Fig. 4** (a) Schematic view of the miniaturized electrochemical cell. (b) Chronoamperometric curve for the electrochemical thinning process.  $E = 1.5$  V vs. Ag/AgCl (c) Sequence of images obtained during the electrochemical process. The height of the electrolyte is approximately 2 mm. (d and e) Pictures of MoS<sub>2</sub> before and after the process. (f) Raman map of the MoS<sub>2</sub> layer. Scale bars for figures d, e, f are 25  $\mu$ m. (g) Schematic illustration of the evolution of MoS<sub>2</sub> flakes during the electrochemical thinning process.

Pan *et al.* connected Au tracks using electron beam lithography process only at the edges of bulk MoS<sub>2</sub> and performed a thinning process using voltammetry.<sup>44</sup> In this lateral contact configuration, where MoS<sub>2</sub> is seated on insulating surface, the thinning process start at the edges, but the thinning yield is low. The thickness of the edges is reduced but large thinned areas are not obtained in this type of electrode configuration. Here, bulk MoS<sub>2</sub> flakes are seated on Au electrodes (bottom contact) achieving higher thinning yields. In addition to the effect of electrode contact, we can also consider the ultra-large aspect ratio reported in this work due to the high affinity of monolayer MoS<sub>2</sub> with the Au substrate.<sup>14,51</sup> In addition, the large-area MoS<sub>2</sub> have more anchoring regions with substrate and allows the preparation of even more complex surfaces, as will be shown ahead.

Finally, as a proof-of-concept, we demonstrated the unprecedented preparation of free-standing and thin MoS<sub>2</sub> layers by electrochemical thinning process. Free-standing MoS<sub>2</sub> has been studied from theoretical aspects<sup>52,53</sup> to experimental approaches. The later have been used to investigate mechanical,<sup>54</sup> optical properties,<sup>55</sup> and electrical features,<sup>56</sup> along with application in biosensing assays.<sup>57</sup> In addition, large free-standing layers holds the promise to work as optical windows

to interface dry and wet environments, enabling new fundamental studies in health and energy fields.<sup>58</sup> In brief, we fabricated flexible conductive microhole-structured Ni meshes electrochemically coated with Au thick films (1.5  $\mu$ m), as recently reported.<sup>59</sup> Fig. 6a and b shows photos of these flexible Au meshes. Microholes separated by 35  $\mu$ m from each other and with a diameter of approximately 18  $\mu$ m can be observed in Fig. 6c. The area between the microholes guaranteed the interaction of MoS<sub>2</sub> with the Au substrate. Fig. 6d and e illustrates optical images of MoS<sub>2</sub> flakes before and after the thinning process, respectively. As confirmed by Raman measurements, the flakes were thinned down to a monolayer on the Au surface in this case.

Interestingly, bulk MoS<sub>2</sub> flakes were also thinned on the region over the microholes, resulting in the formation of mono-bilayer free-standing MoS<sub>2</sub> layers. Remarkably, the free-standing diameter (18  $\mu$ m) is at least four times higher when compared with most studies using MoS<sub>2</sub> mono and few-layer,<sup>37,39,54,60</sup> highlighting the feasibility of the method to create large-area free-standing layers. Tilted SEM analysis with an angle of 54 degrees illustrated in Fig. 6f shows that the microhole located in the center of the image was covered by an ultrathin material. Fig. 6g and h shows secondary electron

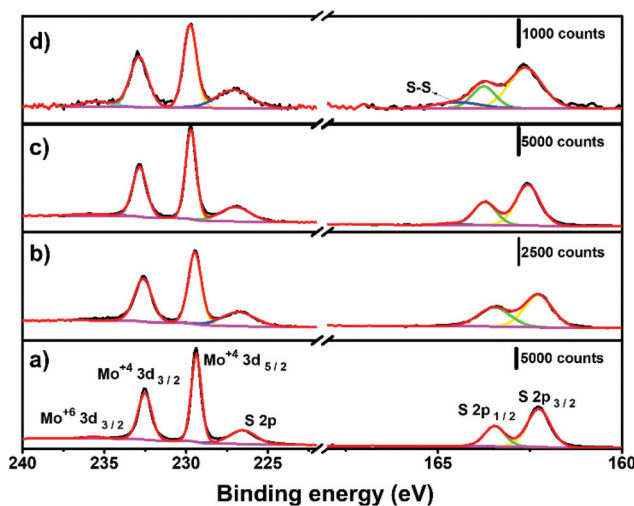


Fig. 5 XPS spectra for (a) bulk  $\text{MoS}_2$  and at different electrochemical thinning times: (b) 5 s, (c) 20 s and (d) 240 s.

SEM and EDS images, respectively. The bulk regions of  $\text{MoS}_2$  are clearly identified by the high intensity pink-red areas in image 6 h. The light pink-red areas show the thinned  $\text{MoS}_2$  regions, including on the center of the microhole.

The region of the  $\text{MoS}_2$  flake over the microhole was selected for additional investigation by Raman spectroscopy, as shown in Fig. 6i and j. The resulting Raman map indicated that the frequency difference ranged from  $19\text{--}21.5\text{ cm}^{-1}$  in some areas, thus confirming that light pink-red areas observed in SEM-EDS images are mono-bilayer regions. In addition, Fig. 6k shows Raman spectra taken in free-standing and supported areas. A red-shift was observed for both  $A_{1g}$  and  $E_{2g}^1$  modes for the spectra obtained over the microhole. This result is in agreement with the Raman spectra reported for free-standing layers on microholes<sup>61</sup> and wrinkled  $\text{MoS}_2$  prepared on elastomeric substrates.<sup>62</sup> Height profiles obtained by AFM indicated that  $\text{MoS}_2$  layer advanced 200–250 nm into deeper regions of the microhole (Fig. S8†), which contributes to create strain in the 2D material. Such phenomenon is likely the cause of this red-shift as noted herein and in the literature for free-standing  $\text{MoS}_2$  layers. In addition, HAADF-HRSTEM image confirmed the presence of mono-bilayer regions, as illustrated in Fig. 6l.

## Conclusions

In this work, we reported a simple and fast electrochemical thinning process to obtain ultra-large  $\text{MoS}_2$  monolayers on Au

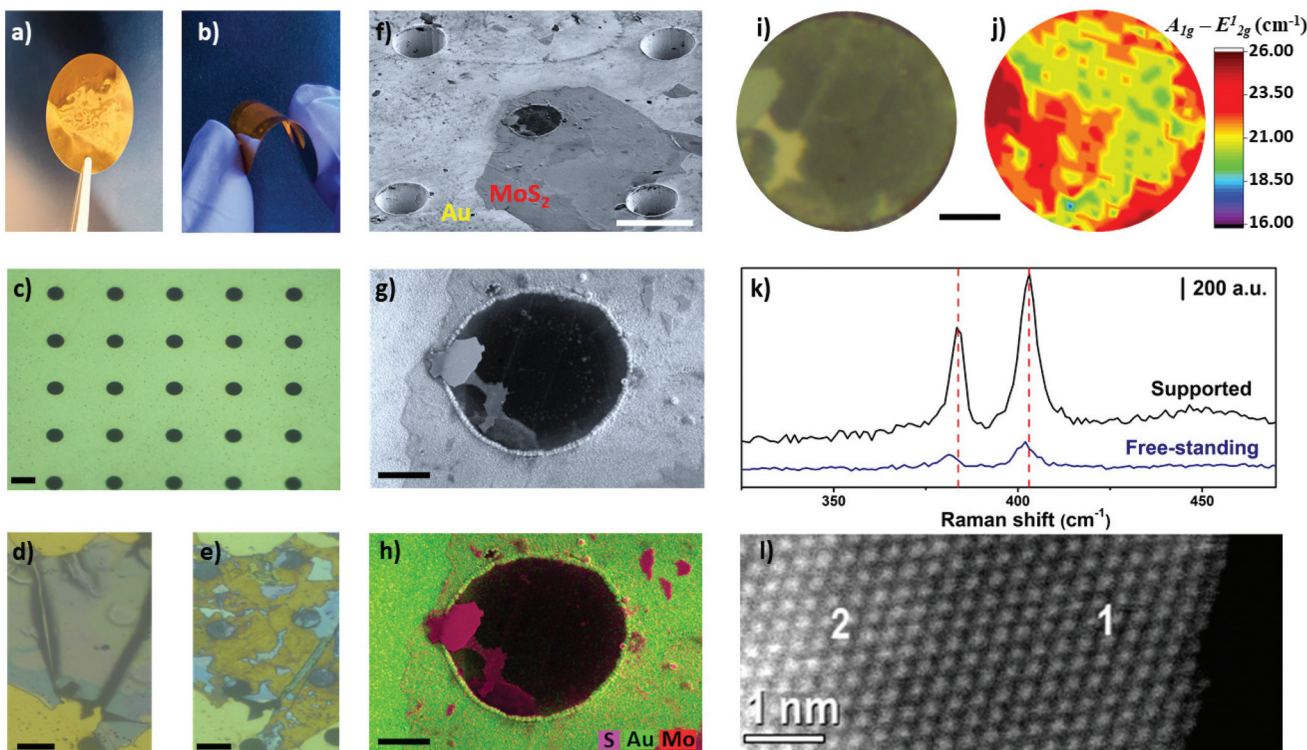


Fig. 6 (a and b) Photos of the microhole-structured Ni/Au mesh. (c) Optical microscopy image of the Au mesh. Scale bar is  $20\text{ }\mu\text{m}$ . (d and e) Optical microscopy images of the  $\text{MoS}_2$  flakes before and after electrochemical thinning process, respectively. Scale bar is  $25\text{ }\mu\text{m}$ . (f) Tilted secondary electron SEM image of the thinned flake on the Au micromesh. Scale bar is  $25\text{ }\mu\text{m}$ . (g and h) High-magnification secondary electron SEM image of thinned area on the microhole and EDS map, respectively. Scale bar is  $5\text{ }\mu\text{m}$ . (i and j) Optical microscope image of the microhole region and Raman map, respectively. Scale bar is  $5\text{ }\mu\text{m}$ . (k) Raman spectra obtained on supported and free-standing areas as indicated. (l) HAADF-HRSTEM image of the electrochemically thinned  $\text{MoS}_2$  layer. The inset numbers 1 and 2 indicated mono and bilayer regions, respectively.

substrates. Bulk MoS<sub>2</sub> flakes transferred to the conductive substrates are thinned down to a monolayer with more than 90% of initial bulk area being removed at potentials in the range of 1.5–1.7 V. The influence of the applied potential was assessed by image treatment, highlighting the possibility to roughly tune the thinning area by controlling oxidation potential. Bulk residues are mainly located at the flake edges while the basal plane presented large-area mono-bilayer regions, as confirmed by atomic force microscopy, photoluminescence and Raman experiments. Real-time visualization of the thinning process was achieved through the hyphenation of optical microscopy and electrochemistry, revealing that the thinning process starts at the edges and moves in the direction of the center of the flake. Moreover, hyphenation of techniques was used to investigate the thinning time, revealing the impact of the process on a wide range of flake sizes. We demonstrated the thinning process in ultra large-area MoS<sub>2</sub> that can reach approximately 813.5 × 411 μm by adjusting the thinning time. Thus, our route is very promising toward preparation of centimeter-scale monolayer MoS<sub>2</sub> that could be used in the field of energy storage, such as lithium–sulfur batteries. Development of those novel energy-storage devices, with high gravimetric energy density beyond the traditional lithium-ion batteries, still demand ways to overcome performance losses due to the dissolution of lithium polysulfides species (Li<sub>2</sub>S<sub>n</sub>,  $n = 4–8$ ) into electrolytes. Yet, the best strategy is to use materials that are able to trap solution Li<sub>2</sub>S<sub>n</sub> intermediates, and MoS<sub>2</sub> monolayers withstand as one of these promising materials due its large surface area and good catalytic activity or the formation and the decomposition of Li<sub>2</sub>S in discharge and charge processes.<sup>63,64</sup>

The preparation of free-standing mono-bilayer MoS<sub>2</sub> using electrochemical thinning from bulk crystals was demonstrated for the first time on Au micromeshes. Despite its preliminary character, the electrochemical thinning process of MoS<sub>2</sub> was found to successfully occur on regions that are not in contact with the conductive substrate, *i.e.*, over microholes, resulting in large free-standing areas. Thus, the proposed work opens up the possibility to study mechanical, optical and electrochemical properties of ultra-large strained MoS<sub>2</sub> layers. In addition, further efforts may extend its applicability to other 2D materials than can be thinned by electrochemical routes.

## Author contributions

N. F. and B. R. F. contributed equally to this work and performed the transfer process, electrochemical thinning and characterization studies. J. B. and C. A. O. performed HRSTEM analysis. M. Strauss helped with Raman and PL measurements. V. M. S. F., M. H. O. P. and A. L. G. designed and prepared the meshes. M. Strauss, R. S. L. and E. R. L. helped with discussions. M. S. conceived the idea, designed the experiments and wrote the manuscript.

## Conflicts of interest

The authors Murilo Santhiago, Nicolli de Freitas and Bianca R. Florindo are listed as inventors on a patent filing application describing this technology.

## Acknowledgements

This work was supported by the Serrapilheira Institute (grant number: Serra-1912-31228). We thank Mariane P. Pereira, Davi H. Camargo, Fabiano E. Montoro, Otávio Berenguel, Carolina P. Torres, Carlos A. R. Costa, and Cleyton A. Biffe for their help in this work with instrumentation and laboratory facilities. We also thank SisNano for the support.

## References

- W. Zheng, Y. Jiang, X. Hu, H. Li, Z. Zeng, X. Wang and A. Pan, *Adv. Opt. Mater.*, 2018, **6**, 1800420.
- Y. Liu, N. O. Weiss, X. Duan, H.-C. Cheng, Y. Huang and X. Duan, *Nat. Rev. Mater.*, 2016, **1**, 16042.
- H. H. Huang, X. Fan, D. J. Singh and W. T. Zheng, *Nanoscale*, 2020, **12**, 1247–1268.
- W. Li, X. Qian and J. Li, *Nat. Rev. Mater.*, 2021, **6**, 829–846.
- C. Yim, V. Passi, M. C. Lemme, G. S. Duesberg, C. Ó. Coileáin, E. Pallecchi, D. Fadil and N. McEvoy, *npj 2D Mater. Appl.*, 2018, **2**, 5.
- T. Tan, X. Jiang, C. Wang, B. Yao and H. Zhang, *Adv. Sci.*, 2020, **7**, 2000058.
- Y. Yuan, H. Lv, Q. Xu, H. Liu and Y. Wang, *Nanoscale*, 2019, **11**, 4318–4327.
- A. Bolotsky, D. Butler, C. Dong, K. Gerace, N. R. Glavin, C. Muratore, J. A. Robinson and A. Ebrahimi, *ACS Nano*, 2019, **13**, 9781–9810.
- Y. He, P. Tang, Z. Hu, Q. He, C. Zhu, L. Wang, Q. Zeng, P. Golani, G. Gao, W. Fu, Z. Huang, C. Gao, J. Xia, X. Wang, X. Wang, C. Zhu, Q. M. Ramasse, A. Zhang, B. An, Y. Zhang, S. Martí-Sánchez, J. R. Morante, L. Wang, B. K. Tay, B. I. Yakobson, A. Trampert, H. Zhang, M. Wu, Q. J. Wang, J. Arbiol and Z. Liu, *Nat. Commun.*, 2020, **11**, 57.
- C. Wu, J. Zhang, X. Tong, P. Yu, J. Xu, J. Wu, Z. M. Wang, J. Lou and Y. Chueh, *Small*, 2019, **15**, 1900578.
- M. S. Sokolikova and C. Mattevi, *Chem. Soc. Rev.*, 2020, **49**, 3952–3980.
- A. T. Hoang, K. Qu, X. Chen and J.-H. Ahn, *Nanoscale*, 2021, **13**, 615–633.
- F. Liu, W. Wu, Y. Bai, S. H. Chae, Q. Li, J. Wang, J. Hone and X.-Y. Zhu, *Science*, 2020, **367**, 903–906.
- M. Velický, G. E. Donnelly, W. R. Hendren, S. McFarland, D. Scullion, W. J. I. DeBenedetti, G. C. Correa, Y. Han, A. J. Wain, M. A. Hines, D. A. Muller, K. S. Novoselov, H. D. Abruna, R. M. Bowman, E. J. G. Santos and F. Huang, *ACS Nano*, 2018, **12**, 10463–10472.

15 Y. Huang, Y.-H. Pan, R. Yang, L.-H. Bao, L. Meng, H.-L. Luo, Y.-Q. Cai, G.-D. Liu, W.-J. Zhao, Z. Zhou, L.-M. Wu, Z.-L. Zhu, M. Huang, L.-W. Liu, L. Liu, P. Cheng, K.-H. Wu, S.-B. Tian, C.-Z. Gu, Y.-G. Shi, Y.-F. Guo, Z. G. Cheng, J.-P. Hu, L. Zhao, G.-H. Yang, E. Sutter, P. Sutter, Y.-L. Wang, W. Ji, X.-J. Zhou and H.-J. Gao, *Nat. Commun.*, 2020, **11**, 2453.

16 Q. Zhang, L. Mei, X. Cao, Y. Tang and Z. Zeng, *J. Mater. Chem. A*, 2020, **8**, 15417–15444.

17 G. Eda, H. Yamaguchi, D. Voiry, T. Fujita, M. Chen and M. Chhowalla, *Nano Lett.*, 2011, **11**, 5111–5116.

18 Á. Coogan and Y. K. Gun'ko, *Mater. Adv.*, 2021, **2**, 146–164.

19 P. Yang, X. Zou, Z. Zhang, M. Hong, J. Shi, S. Chen, J. Shu, L. Zhao, S. Jiang, X. Zhou, Y. Huan, C. Xie, P. Gao, Q. Chen, Q. Zhang, Z. Liu and Y. Zhang, *Nat. Commun.*, 2018, **9**, 979.

20 Y. Huang, J. Wu, X. Xu, Y. Ho, G. Ni, Q. Zou, G. K. W. Koon, W. Zhao, A. H. Castro Neto, G. Eda, C. Shen and B. Özyilmaz, *Nano Res.*, 2013, **6**, 200–207.

21 M. Yamamoto, T. L. Einstein, M. S. Fuhrer and W. G. Cullen, *J. Phys. Chem. C*, 2013, **117**, 25643–25649.

22 Y. Liu, H. Nan, X. Wu, W. Pan, W. Wang, J. Bai, W. Zhao, L. Sun, X. Wang and Z. Ni, *ACS Nano*, 2013, **7**, 4202–4209.

23 K. K. Amara, L. Chu, R. Kumar, M. Toh and G. Eda, *APL Mater.*, 2014, **2**, 092509.

24 Y. Yang, H. Hou, G. Zou, W. Shi, H. Shuai, J. Li and X. Ji, *Nanoscale*, 2019, **11**, 16–33.

25 L. Li, D. Zhang, Y. Gao, J. Deng, Y. Gou and J. Fang, *J. Alloys Compd.*, 2021, **862**, 158551.

26 K. Sunamura, T. R. Page, K. Yoshida, T. Yano and Y. Hayamizu, *J. Mater. Chem. C*, 2016, **4**, 3268–3273.

27 A. Ambrosi and M. Pumera, *Chem. Soc. Rev.*, 2018, **47**, 7213–7224.

28 S. García-Dalí, J. I. Paredes, J. M. Munuera, S. Villar-Rodil, A. Adawy, A. Martínez-Alonso and J. M. D. Tascón, *ACS Appl. Mater. Interfaces*, 2019, **11**, 36991–37003.

29 A. Ambrosi and M. Pumera, *Chem. – Eur. J.*, 2018, **24**, 18551–18555.

30 A. Sebastian, F. Zhang, A. Dodd, D. May-Rawding, H. Liu, T. Zhang, M. Terrones and S. Das, *ACS Nano*, 2019, **13**, 78–86.

31 N. Liu, P. Kim, J. H. Kim, J. H. Ye, S. Kim and C. J. Lee, *ACS Nano*, 2014, **8**, 6902–6910.

32 S. Das, M. K. Bera, S. Tong, B. Narayanan, G. Kamath, A. Mane, A. P. Paulikas, M. R. Antonio, S. K. R. S. Sankaranarayanan and A. K. Roelofs, *Sci. Rep.*, 2016, **6**, 28195.

33 D. S. Schulman, D. May-Rawding, F. Zhang, D. Buzzell, N. Alem and S. Das, *ACS Appl. Mater. Interfaces*, 2018, **10**, 4285–4294.

34 T. Hong, T. Shen, J. Yang, Y. Sun, J. Zhang, H. Pan, Y. Hong, Y. Wang, S. Chen, Y. Zhao and C. F. Guo, *Int. J. Smart. Nano Mater.*, 2020, **11**, 1–10.

35 K.-G. Zhou, F. Withers, Y. Cao, S. Hu, G. Yu and C. Casiraghi, *ACS Nano*, 2014, **8**, 9914–9924.

36 H. Li, Q. Zhang, C. C. R. Yap, B. K. Tay, T. H. T. Edwin, A. Olivier and D. Baillargeat, *Adv. Funct. Mater.*, 2012, **22**, 1385–1390.

37 C. Lee, H. Yan, L. E. Brus, T. F. Heinz, J. Hone and S. Ryu, *ACS Nano*, 2010, **4**, 2695–2700.

38 J. Huang, X. Pan, X. Liao, M. Yan, B. Dunn, W. Luo and L. Mai, *Nanoscale*, 2020, **12**, 9246–9254.

39 K. F. Mak, C. Lee, J. Hone, J. Shan and T. F. Heinz, *Phys. Rev. Lett.*, 2010, **105**, 136805.

40 M. Seol, M. Lee, H. Kim, K. W. Shin, Y. Cho, I. Jeon, M. Jeong, H. Lee, J. Park and H. Shin, *Adv. Mater.*, 2020, **32**, 2003542.

41 J. W. Christopher, B. B. Goldberg and A. K. Swan, *Sci. Rep.*, 2017, **7**, 14062.

42 T. F. D. Fernandes, A. de C. Gadelha, A. P. M. Barboza, R. M. Paniago, L. C. Campos, P. S. Soares Guimarães, P.-L. de Assis and B. R. A. Neves, *2D Mater.*, 2018, **5**, 025018.

43 M. Buscema, G. A. Steele, H. S. J. van der Zant and A. Castellanos-Gomez, *Nano Res.*, 2014, **7**, 561–571.

44 X. Pan, M. Yan, C. Sun, K. Zhao, W. Luo, X. Hong, Y. Zhao, L. Xu and L. Mai, *Adv. Funct. Mater.*, 2021, **31**, 2007840.

45 X. Xu, A. Makaraviciute, J. Pettersson, S.-L. Zhang, L. Nyholm and Z. Zhang, *Sens. Actuators, B*, 2019, **283**, 146–153.

46 J. C. Hoogvliet and W. P. van Bennekom, *Electrochim. Acta*, 2001, **47**, 599–611.

47 J. D. Benck, B. A. Pinaud, Y. Gorlin and T. F. Jaramillo, *PLoS One*, 2014, **9**, e107942.

48 F. Wu, Z. Liu, N. Hawthorne, M. Chandross, Q. Moore, N. Argibay, J. F. Curry and J. D. Batteas, *ACS Nano*, 2020, **14**, 16939–16950.

49 F. Li, F. Gao, M. Xu, X. Liu, X. Zhang, H. Wu and J. Qi, *Adv. Mater. Interfaces*, 2018, **5**, 1800348.

50 R. Ding, Y. Liu, M. Wang, L. Qin, X. Cui, C. Wang, L. Wang and B. Lv, *Electrochim. Acta*, 2017, **248**, 20–28.

51 M. Velický, A. Rodriguez, M. Bouša, A. V. Krayev, M. Vondráček, J. Honolka, M. Ahmadi, G. E. Donnelly, F. Huang, H. D. Abruña, K. S. Novoselov and O. Frank, *J. Phys. Chem. Lett.*, 2020, **11**, 6112–6118.

52 S. Ghaderzadeh, V. Ladygin, M. Ghorbani-Asl, G. Hlawacek, M. Schleberger and A. V. Krasheninnikov, *ACS Appl. Mater. Interfaces*, 2020, **12**, 37454–37463.

53 J. Jiang, L. Wang and Y. Zhang, *J. Appl. Phys.*, 2019, **126**, 135106.

54 S. Manzeli, D. Ovchinnikov, D. Pasquier, O. V. Yazyev and A. Kis, *Nat. Rev. Mater.*, 2017, **2**, 17033.

55 K. Kojima, H. E. Lim, Z. Liu, W. Zhang, T. Saito, Y. Nakanishi, T. Endo, Y. Kobayashi, K. Watanabe, T. Taniguchi, K. Matsuda, Y. Maniwa, Y. Miyauchi and Y. Miyata, *Nanoscale*, 2019, **11**, 12798–12803.

56 W. M. Parkin, A. Balan, L. Liang, P. M. Das, M. Lamparski, C. H. Naylor, J. A. Rodriguez-Manzo, A. T. C. Johnson, V. Meunier and M. Drndić, *ACS Nano*, 2016, **10**, 4134–4142.

57 N. Masurkar, N. K. Thangavel, S. Yurgelevic, S. Varma, G. W. Auner and L. M. Reddy Arava, *Biosens. Bioelectron.*, 2021, **172**, 112724.

58 L. M. Meireles, I. D. Barcelos, G. A. Ferrari, P. A. A. de A. Neves, R. O. Freitas and R. G. Lacerda, *Lab Chip*, 2019, **19**, 3678–3684.

59 G. F. Giordano, V. M. S. Freitas, G. R. Schleider, M. Santhiago, A. L. Gobbi and R. S. Lima, *ACS Appl. Mater. Interfaces*, 2021, **13**, 35914–35923.

60 X. Zhang, R. Zhang, X. Zheng, Y. Zhang, X. Zhang, C. Deng, S. Qin and H. Yang, *Nanomaterials*, 2019, **9**, 796.

61 D. Lloyd, X. Liu, J. W. Christopher, L. Cantley, A. Wadehra, B. L. Kim, B. B. Goldberg, A. K. Swan and J. S. Bunch, *Nano Lett.*, 2016, **16**, 5836–5841.

62 A. Castellanos-Gomez, R. Roldán, E. Cappelluti, M. Buscema, F. Guinea, H. S. J. van der Zant and G. A. Steele, *Nano Lett.*, 2013, **13**, 5361–5366.

63 W. Cui, H. Li, Y. Liu, Q. Cai and J. Zhao, *Physica E*, 2021, **130**, 114715.

64 S. Dong, X. Sun and Z. Wang, *Beilstein J. Nanotechnol.*, 2019, **10**, 774–780.